POLITECNICO DI TORINO
Repository ISTITUZIONALE

Unveiling the acid properties of metallosilicate nanospheres: a combined experimental and computational study

Original
Unveiling the acid properties of metallosilicate nanospheres: a combined experimental and computational study / Maertens, A., Rubirigi, C., Marsala, V., Soumoy, L., Armandi, M., Fiorilli, S., Champagne, B., Aprile, C.. - In: MATERIALS ADVANCES. - ISSN 2633-5409. - 7:14(2026), pp. 7369-7382. [10.1039/D5MA01361E]

Availability:
This version is available at: 11583/3016849 since: 2026-10-21T10:36:32Z

Publisher:
Royal Society of Chemistry - RSC

Published
DOI:10.1039/D5MA01361E

Terms of use:

This article is made available under terms and conditions as specified in the corresponding bibliographic description in the repository

Publisher copyright

(Article begins on next page)

26 October 2026

Materials Advances

ROYAL SOCIETY OF CHEMISTRY

PAPER

Published on 02 July 2026
Licensed under CC-BY-NC 4.0

Check for updates

Cite this: *Mater. Adv.*, 2026, 7, 7369

Unveiling the acid properties of metallosilicate nanospheres: a combined experimental and computational study

Amélie Maertens, †‡[a] Charles Rubirigi, †[b] Vittorio Marsala,[a] Loraine Soumoy,§[a] Marco Armandi,[c] Sonia Fiorilli,[c] Benoît Champagne *[b] and Carmela Aprile *[a]

Received 23rd November 2025, Accepted 28th April 2026

DOI: 10.1039/d5ma01361e

rsc.li/materials-advances

The design of solid acid catalysts with tunable Brønsted and Lewis acidity is essential for biomass valorization reactions. This study explores the synthesis, characterization, and catalytic behavior of extra-small mesoporous aluminosilicate nanospheres for the acetalization of glycerol to solketal. The synthesis was optimized by varying the Si/Al ratio, the nature of the aluminum precursor and the dissolution medium, concluding that ethanol afforded uniform nanospheres with high intra-framework Al incorporation. In-depth characterization *via* TEM, ICP-OES, N_2 physisorption, ^{27}Al ssNMR and FT-IR spectroscopy using NH_3 and CO probes revealed that increasing the Al content enhances overall acidity, particularly Brønsted sites. However, materials with overly strong Brønsted acidity exhibited reduced activity due to too strong interaction with reaction intermediates leading to catalyst poisoning. The aluminosilicate catalyst synthesized using $Al(NO_3)_3$ with a Si/Al ratio of 74 showed the best performance, with a balanced Brønsted/Lewis ratio and moderate acid strength. Comparative studies with gallosilicates and Al–Ga bi-functional materials demonstrated that both Brønsted and Lewis sites contribute synergistically to the reaction path, with optimal performance at an intermediate B/L ratio of 3.5. DFT-based simulations of IR spectra, structure, and deprotonation energies further rationalized the experimental findings, thus providing a solid background for a straightforward structure/activity correlation. These insights offer a set of valuable design principles for the synthesis of advanced heterogeneous acid catalysts.

1. Introduction

The insertion of active single-sites into mesoporous silica networks *via* the isomorphic substitution of Si atoms by trivalent or tetravalent cations has been well documented and largely studied across various structures. This method confers acidic properties to the silica framework and can therefore be highly beneficial for several catalytic processes.[1–5] It is known that the nature of the element inserted into the silica framework can strongly impact the relative amount of Brønsted (B) and Lewis (L) acid sites in the final material, thus influencing catalytic activity. Independently of their nature (Brønsted or Lewis), the strength of the acid sites is also a parameter playing a pivotal role in catalysis. In particular, the introduction of trivalent cations (*e.g.* Al^{3+}, Ga^{3+}) into the silica framework is known to generate a combination of B and L acid sites with a predominant Brønsted character.[6,7] These acidic properties are beneficial for numerous catalytic processes (*e.g.* Diels–Alder,[8–10] ethanol dehydration,[11] isomerization and dimerization of pinene,[12] alkylation of phenol[1,13] or synthesis of (2,2-dimethyl-1,3-dioxolan-4-yl)methanol, also known as solketal[14–16]).

Launey *et al.* reported that a Ga-substituted SBA-15 solid displayed weaker acid sites and a lower B/L ratio compared to its aluminosilicate counterparts, resulting in enhanced catalytic activity for α-pinene isomerization of the former.[17] Gracia *et al.* studied the catalytic activity of Ga- and Al-SBA-15 for the alkylation of toluene through the Friedel–Crafts reaction. They observed that the Al-SBA-15 solid displayed better performances for the alkylation in the presence of benzyl alcohol,

[a] *Laboratoire de Chimie des Matériaux Appliqués, Department of Chemistry, Namur Institute of Structured Matter (NISM), University of Namur, 5000 Namur, Belgium. E-mail: carmela.aprile@unamur.be*

[b] *Laboratoire de Chimie Théorique, Department of Chemistry, Namur Institute of Structured Matter (NISM), University of Namur, 5000 Namur, Belgium. E-mail: benoit.champagne@unamur.be*

[c] *Department of Applied Science and Technology, Politecnico di Torino, 10129 Torino, Italy*

† These authors contributed equally to this work.

‡ Present address: Dow Silicones Belgium, Seneffe, Belgium.

§ Present address: AGC Glass Europe, Gosselies, Belgium.

© 2026 The Author(s). Published by the Royal Society of Chemistry

while Ga-SBA-15 was more active for the reaction with benzyl chloride. These behaviors were attributed to the high concentration of Brønsted acid sites in Al-SBA-15, whereas Ga-SBA-15 exhibited a greater number of Lewis acid sites.[13]

One of the key factors to enhance acidity and therefore the catalytic activity is the correct insertion of the heteroelement inside the SiO_2 network. Tetrahedral sites (*i.e.* fully embedded in the matrix) can display Brønsted or Lewis acid sites while the acidity of octahedral species (*i.e.* extra-framework species-EFS) is not straightforward. While EFS Al species were reported as a Lewis acid source in the context of zeolite (*i.e.* aluminosilicates), it was shown for other trivalent and tetravalent elements (*e.g.* Ga, Hf) that EFS does not generate sufficient or appropriate acidity to act as active sites. The presence of EFS should therefore be minimized to enhance the general acidity of the solid surface. To do so, the optimization of the Si/T ratio (*i.e.* with T = Al in the context of aluminosilicates) was often considered. Aluminum has an ionic radius close to that of silicon (0.39 Å and 0.40 Å for Al^{3+} and Si^{4+}, respectively). The insertion of Al into SiO_2 is therefore facilitated, and the risk of obtaining extra-framework species is minimized. However, reaching a low Si/Al ratio increases the risk of finding two Al atoms sharing the same oxygen atom of the network and therefore reduces the catalytic properties.[18] Several groups also mentioned that the nature of the Al source plays a crucial role in the correct insertion of the element inside the SiO_2 network.[19] It was shown by Klinowski *et al. via* ^{27}Al ssNMR analyses that the nature of the precursor strongly influences the presence of intra-framework species (IFS) *vs.* EFS sites and therefore affects the acid types and strength.[20]

Another parameter that could influence the acidity and the catalytic activity of aluminosilicate solids is the morphology and the structure of the materials. The recent development of extra-small silica porous nanospheres (XS-NS) opened interesting perspectives for catalytic applications, as the limitation caused by diffusion of reagents and products is drastically decreased due to the small particle size.[21] High catalytic activity of Sn and Ga substituted XS-NS was observed in the context of biomass derivative valorization.[21,22] It was recently reported that the B/L ratio varies when considering hollow silica nanotubes and hollow silica nanospheres both embedding similar quantities of gallium as single-sites.[16] Therefore, it is difficult to attribute the variation of acidity and catalytic activity to the nature of the inserted element if different silica structures are at play.

With the growing demand for greener chemical processes, the valorization of biomass derivatives into value-added compounds took a predominant place in catalysis research. Acid solids play a pivotal role in this development. Among the interesting valorization procedures, the conversion of glycerol (propane-1,2,3-triol, *i.e.* mainly produced by the biofuel industry and considered as a waste due to the extensive production of bio-based fuels) into solketal (*i.e.* a cyclic acetal that finds applications as a green solvent or a fuel additive) has been particularly studied and shown to be effective. It displays a particularly high atom-economy of 88%, produces only water as a byproduct and usually offers a high selectivity. Several groups reported the high catalytic performances of silica based mesoporous materials embedding tetrahedral sites as active catalysts for this reaction.[14,16,22–24] It was previously reported that this reaction can be activated by both L and B acids but is mainly influenced by Brønsted acidity. Recent studies on gallium- and hafnium-based silica nanospheres and nanotubes attributed the high catalytic activity of these solids to their appropriate B/L balance, which favored Brønsted acid sites.[15,22] However, although glycerol-to-solketal conversion has been widely investigated over several classes of solid acids, reports specifically involving nanosized mesoporous aluminosilicates remain scarce.[25,26] Moreover, the precise role played by the high Brønsted acid population and its relative strength in this reaction was not explored in depth.

Herein, the synthesis of silica porous nanospheres with extra-small size (<100 nm) embedding aluminum as single sites was successfully achieved. The role of the Al sources in the morphology, structure, and acidity of the materials was investigated by means of various characterization methods including transmission electron microscopy (TEM), N_2 physisorption, and ^{27}Al solid state nuclear magnetic resonance (ssNMR). The catalytic activity of the different solids was evaluated for the conversion of glycerol to solketal. The Si/Al ratio was also optimized and its impact on the nature and the strength of the acid site population was studied in depth by means of Fourier transform infrared (FT-IR) measurement of NH_3 and CO adsorption. To shed light on the specific role of the trivalent heteroelement, the optimized nanosized porous aluminosilicate was compared with its analogous gallosilicate material. In addition, bifunctional solids embedding simultaneously gallium and aluminum single-sites were synthesized and characterized in order to enhance the understanding of the precise influence of both the Brønsted over Lewis ratio and the relative strength of the active sites. It deserves to be mentioned that the role played by Brønsted and Lewis acid sites in the catalytic activity was understood in depth through a direct comparison of a series of catalysts that share the same morphology, porosity, particle size, and a very similar specific surface area, while differing in their acidity. Moreover, a computational investigation based on the evaluation of both spectroscopic (FT-IR) and structural features was performed on Al and Ga-silicates. To complete the scenario, the deprotonation energy was evaluated as well. This combined experimental and computational approach allows unveiling a complete picture of the acid sites.

2. Experimental

2.1. Materials

Cetyltriammonium bromide (CTAB) and tetraethoxysilane (TEOS) were purchased from TCI, NH_4OH (30%), gallium nitrate and acetone were obtained from Carl Roth, aluminum chloride, aluminum nitrate, aluminum isopropoxide, and glycerol (propane-1,2,3-triol) were purchased from Sigma-Aldrich.

 © 2026 The Author(s). Published by the Royal Society of Chemistry

2.2. Catalyst synthesis

The protocol is based on the work of Aprile *et al.*[21,22] and adapted to the use of aluminum. In a polypropylene bottle, CTAB (656.0 mg, 1.8 mmol) is added to Milli-Q water (314 mL, 17.4 mol). The solution is stirred at 800 rpm until complete dissolution, NH_4OH (Carl Roth 30%, 1.0 g, 8.6 mmol) is added, then the solution is stirred for 30 min at room temperature (RT). Aluminum nitrate, aluminum chloride, and gallium nitrate are dissolved in 1 mL of absolute ethanol. Aluminum isopropoxide is dissolved in 3 mL of HNO_3 0.15 M at 50 °C for 2 h. The inorganic precursor solution is added dropwise to the basic medium simultaneously with TEOS (3.0 g, 14.4 mmol). The mixture is stirred for 30 min at RT. The amount of Al and Ga precursor used depends on the targeted Si/Al ratio (74, 37, 18). The obtained white solid is filtered and washed three times with EtOH and distilled H_2O. It is dried overnight at 65 °C and calcined in air at 550 °C, 5 h, rate: 2 °C min^{-1}. Molecular composition: (TEOS: 1/Al precursor: $x/Ga(NO_3)_3{\cdot}xH_2O$: y/H_2O: 1211/CTAB: 0.125/NH_4OH: 0.60), where x varies with the Si/Al ratio.

2.3. Catalytic tests

The freshly calcined catalyst (30.0 mg) is added to the glycerol (920.9 mg, 10.0 mmol) in a 10 mL round bottom flask. Acetone (2.32 g, 40.0 mmol) is added, and the mixture is stirred at 800 rpm at 50 °C for 2 h. After the reaction, 3 mL of absolute ethanol is added. The solution is centrifuged to separate the catalyst. The supernatant is separated, solvents are evaporated under vacuum and the mixture is analyzed by ^1H NMR with DMSO-d6 as a deuterated solvent. The yield of solketal is determined by integrating the peaks corresponding to the hydroxyl groups of the glycerol, the solketal, and the major by-product, a six-membered ring.

2.4. Characterization

Transmission electron microscopy (TEM) pictures were captured with a Philips Tecnai 10 device operating at 100 kV. Samples were dispersed in absolute ethanol and deposited on a Formvar-Copper grid. The total Al and Ga content of the samples was determined *via* inductively coupled plasma optical emission spectroscopy (ICP-OES) on an Optima 8000 Spectrometer. N_2 adsorption–desorption analyses were performed with a Micromeritics ASAP 2420 volumetric adsorption analyzer at 77 K. Before the analysis, a degas treatment (8 h, 150 °C) was applied to the sample under reduced pressure (0.1 mbar). The Brunauer–Emmett–Teller (BET) method was applied in the 0.05–0.30 P/P_0 range to evaluate the specific surface area. The pore size distributions (PSD) were assessed with the density functional theory method using cylinder geometry and N_2-cylindrical pores-oxide surface.[27]

Solid-state NMR of ^{27}Al analyses were performed on a Varian VNMRS 400 spectrometer operating at 9.4 T equipped with a 4 mm Chemagnetics probe. The samples were packed in a 4 mm zirconia rotor and spun at a spinning frequency of 8000 Hz. Spectra were recorded with a one-pulse sequence without ^1H decoupling, a relaxation delay of 0.2 s, an excitation pulse of 0.5 μs (9°) and 5.0 ms acquisition time.

Magic angle spinning (MAS) ssNMR spectra were analyzed by lineshape deconvolution using the software "dmfit"[28] using Lorentzian functions. Prior to fitting, all the spectra were phase-corrected, the baseline was adjusted, and a line broadening of 20 Hz was applied.

FT-IR measurements were conducted using a Bruker Tensor 27 spectrometer equipped with a liquid nitrogen-cooled mercury–cadmium–telluride (MCT) detector, operating at a 2 cm^{-1} resolution in transmission mode. A standard vacuum frame was employed for thermal pre-treatment and dosing of probe molecules in an IR cell supplied with KBr windows. The samples were pressed into self-standing wafers and outgassed for 1 hour (residual pressure <0.1 Pa) at 400 °C prior to probe dosing.

Activated samples were exposed to increasing dosages of ammonia, reaching a maximum equilibrium pressure of 30 mbar, with spectra recorded after each dose. The ammonia equilibrium pressure was then gradually decreased, and the samples were outgassed for approximately 30 min.

For CO adsorption experiments, the samples were outgassed at the same temperature and then exposed to 30 mbar of carbon monoxide equilibrium pressure. Spectra were recorded at room temperature, and then liquid nitrogen was poured into the FT-IR cell to decrease the temperature to the nominal temperature of 77 K. FT-IR spectra were recorded until no further modifications were observed in the intensity of the FT-IR signals. Subsequently through the gradual expansion of the gas in the cell, the CO equilibrium pressure was decreased and the related FT-IR spectrum was recorded.

The recorded spectra were normalized relative to the integrated adsorption of silica framework overtone bands, considering the use of wafers with similar optical density (approximately 5 mg cm^{-2}). These spectra are presented as difference spectra, obtained by subtracting the IR spectrum of the sample before adsorption of probe molecules.

2.5. Computational methods

Due to their amorphous structure, the catalysts studied in this work do not have a well-defined structure. Therefore, quantum chemistry calculations (QM) have been performed on small models using a "cluster" approach. In this approach, acid sites are modeled as hemispherical clusters. To account for the diversity of the amorphous framework, several hemispheres are cut from the starting silica structure. The protocol employed for this work combines molecular dynamics (MD) and quantum chemistry. It has been shown to be efficient to compute the chemical properties of Brønsted aluminosilicate clusters (Fig. S1).[29] These models were created by carving 9 Å hemispheres at the surface of an amorphous silica slab generated by molecular dynamics. After carving, terminal Si atoms were deleted and the Si–O dangling bonds were capped with hydrogen atoms. Vandervelden *et al.*[30] showed that in such sequential MD-then-QM procedures, the initial MD structure could lead to some artifacts in the QM results. Therefore, they

© 2026 The Author(s). Published by the Royal Society of Chemistry

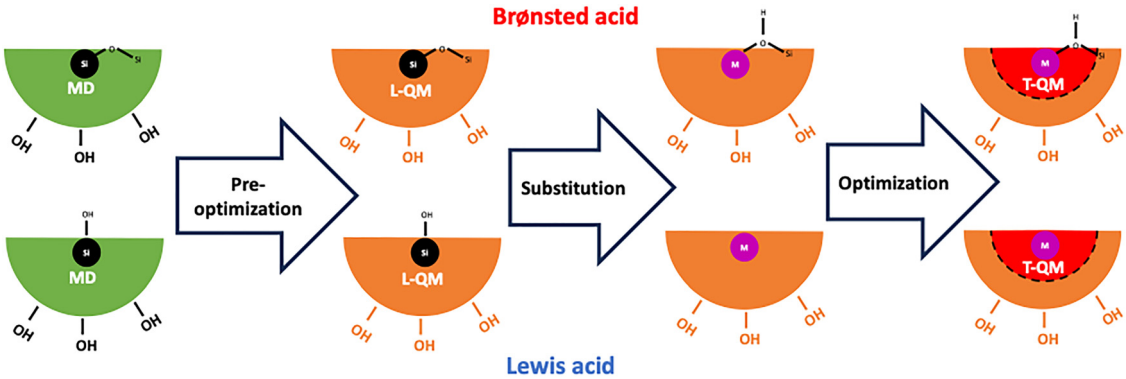

Fig. 1 QM-Opt protocol to optimize the geometry of a silica cluster generated from MD (green), doped with a heteroelement (M = Al, Ga) adapted from Vandervelden *et al.*[30] A 9 Å hemisphere is first extracted from an amorphous silica slab generated with MD. The cluster is saturated with O–H groups and "pre-optimized" at the DFT level with a loose convergence criterion (orange). Brønsted acid sites are modeled by substituting a silicon atom with a heteroelement (Al or Ga) and adding a proton as a balancing charge on a neighboring oxygen. Lewis acid sites are modeled by substituting a silicon atom bearing one hydroxyl group (isolated silanol). The hydroxyl group is removed to yield a tri-coordinated metal. The central atom is then replaced by a heteroelement. The geometry of the acid site is finally optimized with a tighter convergence criterion (red), where only atoms close to the active site are allowed to move (delimited with dotted lines).

designed a multi-step protocol to limit the influence of this so-called "procedural disorder". This starts with a pre-optimization step, where the structure is first fully relaxed at the density functional theory (DFT) level. In this step, a "loose" convergence criterion is applied to reach an equilibrium geometry more quickly. Then, the acid site is created by substituting the central silicon atom with a heteroelement (M = Al or Ga). Those "doped" clusters are "sliced" into tetrahedral atoms (Si or M) layers. The first layer corresponds to the aluminum (or gallium) atom and its neighboring oxygen atoms, the second layer corresponds to the following silicon atoms and their neighboring oxygen atoms, and so on. This protocol ends with a second geometry optimization step, where only atoms in the first three layers are allowed to move (Fig. 1). Here a "tight" convergence criterion is applied to obtain the final structure. For the study of ammonia adsorption, an NH_3 molecule was placed at a 2 Å distance above the acid site as the starting geometry. Along with the complex catalyst-probe optimization, the probe molecule was allowed to move, and the frozen region was kept the same as for geometry optimization.

The environment of the silicon atom chosen as the center of the half-sphere defines the nature of the site to be modeled. A Lewis acid site is modeled from a silicon atom bearing one hydroxyl group (mono-silanol). This silicon atom is replaced by the targeted heteroelement, and the hydroxyl group is removed to produce a tri-coordinated Lewis acid site. For Brønsted acid sites, a silicon atom at the surface bonded to four oxygen atoms, themselves bonded to silicon atoms, is selected. After the substitution by the heteroelement, a proton is added to a neighboring oxygen as balancing charge (Fig. 1). Several clusters must be built in order to simulate the amorphous character of the catalyst. Respectively, 12 and 11 Brønsted and Lewis acid site models have been used in this work.

To simulate the IR spectrum of the NH_3 adsorbed clusters, vibrational frequency calculations were performed providing also the IR transition intensities. To avoid imaginary frequencies, the initial frozen region was kept the same, even though it does not impact the normal modes in the region of interest. The frequencies have been scaled with an empirical scaling factor of 0.94 to fit the experimental spectrum. Following the procedure used by Jystad *et al.*,[31] the IR spectrum of each acid site was simulated by applying a Gaussian broadening of 30 cm^{-1} to each transition. This is done to account for anharmonicity effects. Finally, the spectrum was obtained by summing each contribution and normalizing over the total number of Lewis and Brønsted acid sites. This allowed the signature of both acid types to be assessed. All quantum chemistry calculations were performed with the GAUSSIAN16 software.[32] During the pre-optimization step, the B3LYP XC functional and the 6-311G* basis set are used. The D3 dispersion corrections were included in this last geometry optimization.[33] When the central silicon atom was replaced by a Ga atom, it was described by the def2-TZVPP basis set.[34]

3. Results and discussion

3.1. Optimization of the synthesis parameters

Prior to the in-depth investigation of the acid properties, a series of materials was synthesized to optimize the isomorphic substitution of Si with Al. Indeed, the insertion of Al in the silica framework is known to generate a combination of B and L acid sites with a predominant Brønsted character. B acid sites originate from various acidic hydroxyl groups, including both free silanols near aluminum atoms and bridged Si(OH)Al groups. In contrast, L acid sites arise from coordinatively unsaturated aluminum centers created by the isomorphous substitution of Si^{4+} with Al^{3+}, which introduces local electron-deficient environments capable of accepting electron pairs. Extra-framework Al species (EFS) were also reported as a Lewis acid source in the context of zeolite (*i.e.* aluminosilicates). However, it was shown for other trivalent and tetravalent

 © 2026 The Author(s). Published by the Royal Society of Chemistry

elements (*e.g.* Ga, Hf) that EFS does not generate sufficient acidity to catalyze the conversion of glycerol to solketal.[15,35] The presence of EFS should therefore be minimized.

To optimize the insertion of Al in tetrahedral coordination within the SiO_2 architecture, the tuning of two parameters was considered: (i) the nature of the Al precursor and (ii) the Al content (through the optimization of the Si/Al ratio). To investigate the role played by the Al source, a series of three materials were synthesized employing aluminum nitrate, aluminum chloride, and aluminum isopropoxide. The solids were labeled Al–NS–Nit, Al–NS–Cl, and Al–NS–Iso, respectively. As previously observed with silica nanospheres bearing indium as a single-site, the solubilization of the inorganic precursors is a crucial step to obtain spherical particles of extra-small size.[19] If the precursor requires an acidic medium to be efficiently solubilized, it results in the formation of inhomogeneous aggregates of particles. In the context of aluminosilicates, aluminum nitrate and aluminum chloride were solubilized in absolute ethanol while an aqueous solution of HNO_3 0.15 M was required to obtain a stable solution of aluminum isopropoxide. Based on previously reported data,[15,19,22] a Si/Al ratio of 74 was targeted for this first series of materials. This ratio was identified as optimal to maximize the insertion while reducing the quantity of extra-framework species.

Transmission electron microscopy was used to investigate the morphology of the solids. Fig. 2-I and -II shows that Al–NS–Nit and Al–NS–Cl display spherical particles of homogeneous shape and size. Extra-small particles (particle diameter of *ca.* 25 nm) were observed as confirmed by the particle size distribution (see Fig. S2). In contrast, Al–NS–Iso displays aggregates of bigger particle size (Fig. 2-III) which could be ascribed to the acid medium employed to solubilize the precursor. To confirm this hypothesis, an additional material was synthesized under similar conditions to Al–NS–Nit but dissolving aluminum nitrate in HNO_3 0.15 M. The new material (Al–NS–Nit-a) shows non-homogeneous aggregates of larger particles displaying irregular shape (Fig. 2-IV and Fig. S3). This result confirms that the lack of sphericity and homogeneity cannot be ascribed to the nature of the Al precursor but to the additional presence of an acid solution in the synthesis medium. These observations are in good consistency with the results reported for indo-silicates.[19]

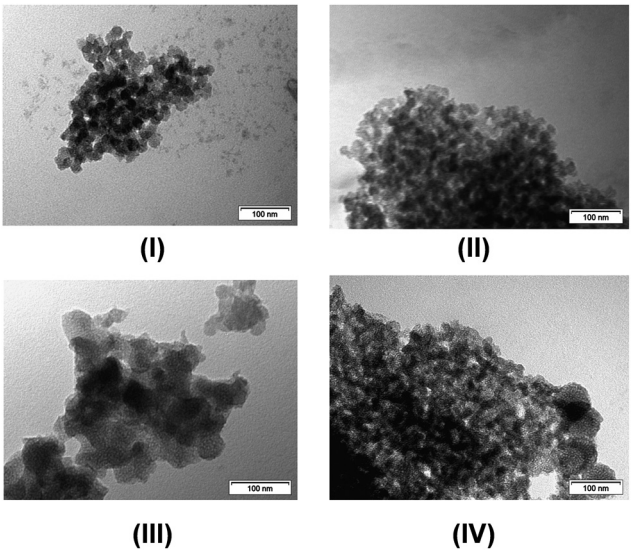

Fig. 2 TEM images of aluminosilicate nanospheres synthesized with different precursors. (I) Al–NS–Nit, (II) Al–NS–Cl, (III) Al–NS–Iso and (IV) Al–NS–Nit-a.

All the samples display a high Brunauer–Emmett–Teller (BET) specific surface area (*i.e.* >1000 m^2 g^{-1}) assessed by N_2 physisorption (Table 1). The adsorption–desorption isotherms of the four silicates are shown in Fig. 3 and display a type IVa isotherm, typical of mesoporous silica materials. The hysteresis present on each isotherm can be described as type H-1 according to the IUPAC definition.[36] Such features are generally observed with porous materials composed of agglomerates of uniform spheres with a narrow pore size distribution.[37] The latter was evaluated by density functional theory since the traditionally used Barrett–Joyner–Halenda (BJH) interpretation is not suitable for the analysis of small mesopores (*i.e.* <4 nm). All the materials display a narrow distribution centered around 3.5 nm.

The total amount of aluminum present in the solids was quantified by ICP-OES analysis. The results obtained match the targeted Si/Al ratio of 74 for all samples (Table 1). However, ICP analyses determine the total quantity of Al but do not provide any insight into its coordination environment.

To shed more light on this parameter, the samples were analyzed *via* ^{27}Al solid-state nuclear magnetic resonance. Tetrahedrally coordinated Al atoms are known to produce a contribution centered at *c.a.* 60 ppm. The precise chemical shift depends on the environment of Al and can be attributed to $Al(OH)_{4-n}(OSi)_n$ species corresponding to aluminum atoms fully embedded in the silica structure.[38] Al atoms within an octahedral coordination extra-framework species are known to produce a signal at 0 ppm.[39]

The four solids display an intense band centered around 60 ppm corresponding to intra-framework Al fully inserted in the SiO_2 network (Fig. 4). The signal ascribed to octahedral Al at 0 ppm is also visible, indicating the presence of some extra-framework species. The proportion of intra-framework (Al(IV)) species is clearly influenced by the solubilization medium of the Al precursor (Fig. S2 and Table S1). From Fig. 4 and Fig. S4 and Table S1, it emerges that Al–NS–Cl and Al–NS–Nit present a higher proportion of intra-framework (Al(IV)) species while both Al–NS–Iso and Al–NS–Nit-a display a more important overall

Table 1 Physico-chemical properties of aluminosilicate nanospheres synthesized with different precursors

Sample	Precursor	Dissolution medium	Si/Al ICP-OES	S_{BET} (m^2 g^{-1})	DFT pore size (nm)
Al–NS–Nit	$Al(NO_3)_3$	EtOH	77	1240	3.2
Al–NS–Cl	$AlCl_3$	EtOH	75	1254	3.3
Al–NS–Iso	$Al(O\text{-}i\text{-}Pr)_3$	HNO_3	74	1232	3.2
Al–NS–Nit-a	$Al(NO_3)_3$	HNO_3	70	1124	3.4

© 2026 The Author(s). Published by the Royal Society of Chemistry

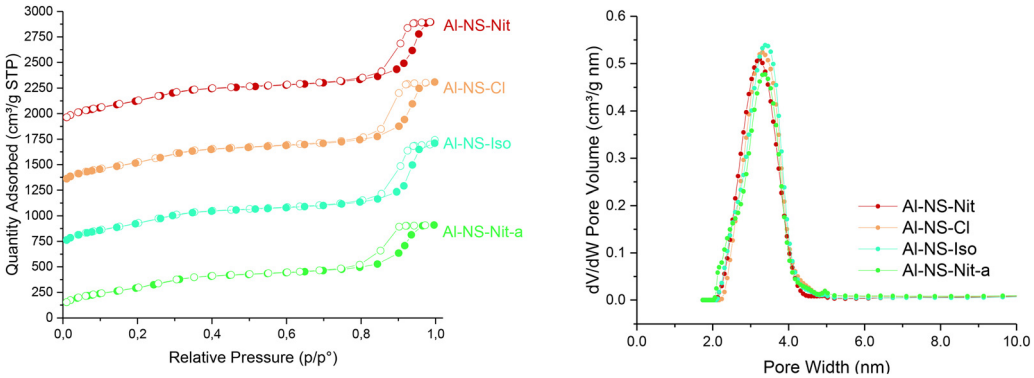

Fig. 3 N_2 physisorption adsorption–desorption isotherm (left) and DFT pore size distribution (right) of four aluminosilicates nanospheres synthesized with various Al sources. The isotherms of Al–NS–Iso, Al–NS–Cl, and Al–NS–Nit were incremented by 600, 1200 and 1800 $cm^3\ g^{-1}$, respectively, for clarity.

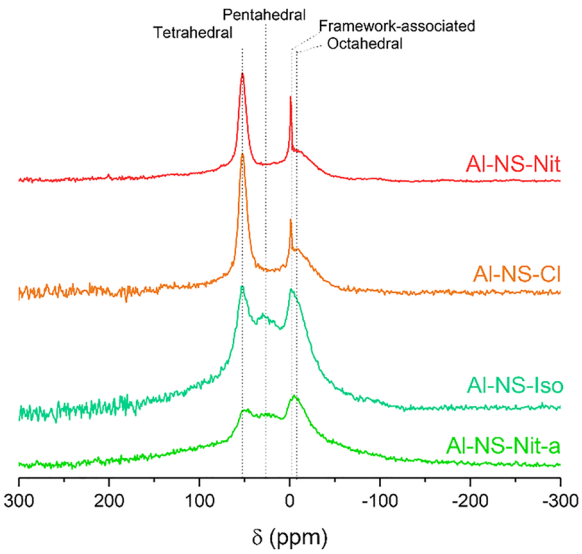

Fig. 4 ^{27}Al solid-state NMR spectra of aluminosilicate nanospheres using different Al sources.

contribution related to extra-framework (Al(VI)) plus penta-coordinated species (Al(V)). Interestingly, a sharp contribution, rarely encountered in aluminosilicate solids, is overlapping the region of extra-framework aluminum for both Al–NS–Nit and Al–NS–Cl. According to the literature, the presence of two signals in the region at *c.a.* 0 ppm can be ascribed to two overlapping contributions related to well-ordered octahedral aluminum (fully extra-framework) and distorted octahedral aluminum (framework associated species). The latter are considered as octahedral aluminum partially inserted in the silica framework that can switch to a tetrahedral environment only under specific conditions (*e.g.* under vacuum at high temperature). According to previous results, such species do not contribute to the Brønsted character, and no clear correlation with Lewis sites was evidenced.[6,40,41] Al–NS–Iso and Al–NS–Nit-a also display an additional broad contribution centered at *c.a.* 30 ppm attributed to penta-coordinated aluminum (see Table S1). The presence of such species is possible in amorphous silica and is generally ascribed to distorted intra-framework Al species[42] or to surface tetrahedral Al coordinating one molecule of water. To better understand the nature of this additional contribution, a ssNMR analysis was performed after dehydrating the sample at 65 °C under vacuum to remove physisorbed water (Fig. S5). The spectrum obtained was still showing the band at 30 ppm, supporting the assignment of this signal to distorted intra-framework Al species. Therefore, it can be concluded that the presence of acid to dissolve the Al precursor not only impacts the morphology of the nanospheres but also the insertion of Al into the silica matrix. For this reason, both samples (*i.e.* Al–NS–Iso and Al–NS–Nit-a) were excluded from further consideration.

Since Al–NS–Nit and Al–NS–Cl present similar structural and textural properties as well as comparable morphologies, the influence of the Si/Al ratio was investigated by selecting Al–NS–Nit as the target material. To study this parameter, two additional solids were synthesized with a Si/Al ratio of 37 and 18 (*i.e.* respectively, twice and four times the quantity of Al in comparison with the initial ratio of 74). The obtained materials were characterized using similar techniques as previously presented, and the results are compared with Al–NS–Nit, renamed hereafter as Al–NS–Nit-74.

ICP-OES showed Si/Al ratios close to the nominal values (Table 2). The N_2 physisorption highlighted the typical type IVa adsorption–desorption isotherm with the expected hysteresis loop (Fig. S6). The DFT pore size was centered around 3 nm (Fig. S6) for all the samples while the specific surface area (SSA) was slightly influenced by the amount of aluminum. Indeed, SSA decreased with the increase in the Al content (Table 2). This observation can be explained by a distortion of the network induced by the elevated amount of aluminum or by the presence of large EFS Al clusters partially clogging the pores.

Table 2 Physico-chemical properties of aluminosilicate nanospheres synthesized with different Si/Al ratios

Samples	Si/Al ICP-OES ratio	S_{BET} ($m^2\ g^{-1}$)	DFT pore size (nm)
Al–NS–Nit-18	18	934	3.0
Al–NS–Nit-37	39	1138	3.0
Al–NS–Nit-74	77	1240	3.3

© 2026 The Author(s). Published by the Royal Society of Chemistry

However, none of these hypotheses could be confirmed *via* TEM investigation. From a morphological point of view, both Al–NS–Nit-37 and -18 were characterized by spherical particles of homogeneous shape and extra-small size, similar to Al–NS–Nit-74 (Fig. S7).

To assess if increasing the Al content influences the proportion between intra and extra-framework species, ^{27}Al ssNMR analyses were conducted as well and the spectra obtained were compared with Al–NS–Nit-74 presented above. Surprisingly, the contribution attributed to intra-framework species (*i.e.* contribution centered at 0 ppm) is not significantly modified as a function of the different Si/Al ratio (Fig. 5 and Fig. S8 and Table S1). It should be noted that the spectra recorded are semi-quantitative. The narrow signal attributed to framework-associated species (*i.e.* surface extra-framework species that can switch to tetrahedral coordination) is less evident for samples Al–NS–Nit-18 and -37. Therefore, for these two solids, most of the octahedral Al seems to belong to extra-framework species. This result, even if only semi-quantitative, suggests that the limitation on the insertion of aluminum is not linked to the quantity involved but to the synthetic conditions. Regardless of the quantity of Al used, a similar proportion is inserted while the excess stays out of the silica matrix.

To verify this hypothesis, both Lewis and Brønsted acid sites of the three Al–NS–Nit samples were investigated by means of FTIR spectroscopy of both adsorbed NH_3 (at room temperature) and CO (at 77 K). Fig. S9 shows the comparison of the normalized difference spectra (*i.e.* the spectrum of the bare sample has been subtracted) registered after NH_3 dosages and prolonged RT outgassing (*ca.* 30 min). This analysis allows evidencing the bands ascribable to species irreversibly formed upon interaction with ammonia.

Fig. 6 shows the bending region between 1800 and 1300 cm^{-1}, where the signals of the ammonia molecule adsorbed on

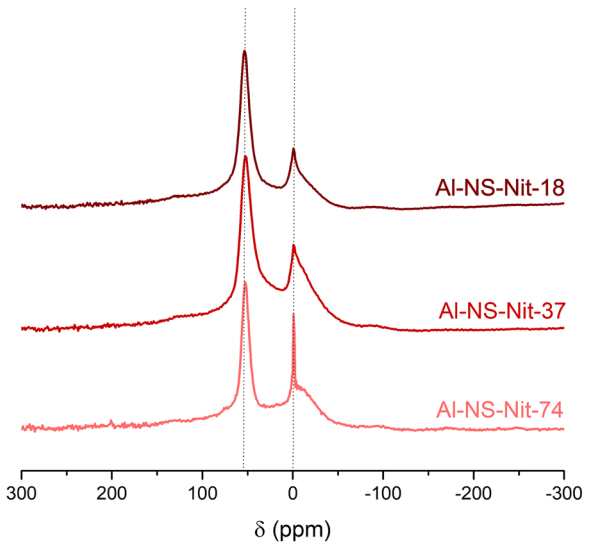

Fig. 5 ^{27}Al ssNMR spectra of aluminosilicate samples with various Si/Al ratios. The dotted lines are indicative of the position of the major contributions.

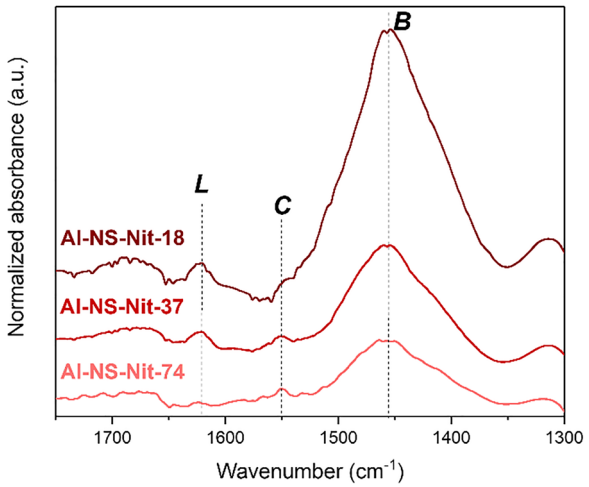

Fig. 6 Normalized difference FT-IR spectra (1800–1300 cm^{-1} frequency region) registered after ammonia dosages and prolonged outgassing at r.t. to evidence the irreversibly adsorbed species on Al–NS–Nit-74, Al–NS–Nit-37, and Al–NS–Nit-18 (L: Lewis, B: Brønsted, C: Chemisorbed ammonia).

Brønsted acid sites resulting in the formation of NH_4^+, and (to a minor extent) on Lewis sites are recognizable. The broad band (labelled with B) at around 1456 cm^{-1} is attributed to the bending mode of NH_4^+ species resulting from the protonation of ammonia from acidic hydroxyl groups.

The integrated absorbance of the band significantly increases with Al content, suggesting that the isomorphous substitution of a higher amount of Al provides a larger source of Brønsted acidity. On the other hand, the band at 1620 cm^{-1} is attributed to ammonia adsorbed onto surface L acid sites, which can be identified as tri-coordinated Al atoms exposed at the surface. This band is rather weak for Al–NS–Nit-74, while increasing slightly for the two other samples. Finally, the band centered at around 1550 cm^{-1} (C) is assigned to N–H bending vibration of Si–NH_2 species formed through the reaction of strained siloxane bridges with ammonia, as previously observed for analogue systems.[15]

FT-IR of ammonia dosages highlights that the increase in Al results in an overall increase in the population of acid sites, with a significantly larger effect on Brønsted acidity. However, due to the relatively strong basicity of ammonia, any potential differences between the three investigated samples regarding the strength of both Lewis and Brønsted acidity cannot be appreciated based on these results. Additionally, the uncertainty related to the calculation of integrated areas for B and L signals, due to the width of the absorption bands, the extremely low quantity of Lewis sites and the presence of other signals that can substantially modify the baseline, did not allow a reliable semi-quantitative evaluation of the B/L ratio for the three samples. Therefore, although these analyses were useful for an initial comparison, adsorption of carbon monoxide at room temperature followed by cooling the sample to nominal 77 K provided additional insights on the surface properties of the investigated solids. CO as a molecular probe is a weaker base than ammonia; hence it is significantly more sensitive to

© 2026 The Author(s). Published by the Royal Society of Chemistry

differences in the acidic strength of L and B sites, based on the spectroscopic changes induced by the interaction with surface species, both in the OH stretching region and in the CO stretching region.

Indeed, the wavenumbers of both ν(CO) and ν(OH) bands can be related directly to the acidic strength of Lewis sites or hydroxyl groups. Upon CO interaction with OH groups, the ν(OH) band is perturbed (*i.e.* shifted towards lower wavenumbers), and the extent of perturbation (*i.e.* $\Delta\nu$OH) is proportional to the OH group acidity. Interestingly, the $\Delta\nu$OH values were found to correlate with the ν(CO) frequency for many zeolites and aluminosilicates.[43,44] Thus, comparing these values for the three samples is considered a reliable method for assessing the acidic strength of OH groups.

Fig. S10 shows the FT-IR spectra of the three samples after CO dosage at room temperature. Besides the typical roto-vibrational profile of the gas molecules present in the three spectra, a significant difference is observed around 2226 cm^{-1}. This band is attributed to CO molecules adsorbed on Lewis sites, whose interaction strength is sufficient to be noticeable at room temperature (labelled as L_S). This evidences that at variance with Al–NS–Nit-74, both Al–NS–Nit-37 and Al–NS–Nit-18 show highly tri-coordinated Al sites acting as strong Lewis, most likely located at the surface of extra small extra-framework clusters. The unexpectedly lower amount of detected Lewis sites (L_S) for Al–NS–Nit-18, which contains a higher amount of aluminum, can be explained by assuming a slight size increase of extra framework clusters resulting in a lower surface-to-volume ratio and fewer exposed aluminum sites.

Additional FT-IR spectra were recorded at the nominal temperature of 77 K to detect the adsorption of CO on Brønsted and (medium and weak) Lewis sites. The interaction with the probe is only enabled at low temperature due to the intrinsically lower acidic strength of CO as a molecular probe compared to NH_3. In the related spectra, reported as normalized difference spectra, both in the frequency region of OH stretching (Fig. 7a) and CO stretching (Fig. 7b), the most relevant spectroscopic changes were detected upon CO adsorption. For clarity and to allow a direct comparison of the observed bands, the figure reports the difference spectra (negative bands are those consumed along interaction with CO) registered for the three samples in contact with the same equilibrium pressure of CO. The high frequency region shows the negative band (3747–3650 cm^{-1}) associated with the erosion of hydroxyl groups and the concomitant appearance of a broad envelope at lower frequency due to OH perturbed upon interaction with CO molecules. These envelopes contain several components, different for the three samples, at equal CO equilibrium pressure, the presence of hydroxyl groups with different acidic strength and in different relative ratios.

Based on the extensive spectroscopic study on the acidic sites of amorphous silica alumina reported by Crépeau *et al.*,[44] three main components can be distinguished, associated respectively to the interaction of CO with free silanols (3656 cm^{-1}), with medium (B_M, 3560 cm^{-1}) and strong Brønsted (3440 cm^{-1}, B_S) sites. The comparison of the three spectra highlights that on equal CO pressure, the component ascribed to B_S sites is predominant for Al–NS–Nit-18, suggesting a relative higher population of stronger acidic sites for the sample with higher Al amounts. This conclusion is also supported by the inspection of the low frequency region (Fig. 7b), where the relative intensities of the signals suggest differences in the strength of probed acidic sites. The signal ascribed to strong Lewis sites is higher for sample Al–NS–Nit-37, confirming the higher population of strong Lewis sites already reported for CO dosed at room temperature. The signal at 2174 cm^{-1}, more intense for Al–NS–Nit-18, is attributed to B_S, confirming a higher population of stronger B sites for this sample compared to the other two solids. The signal is highly asymmetric towards the lower frequency, suggesting a further non clearly discernable component at around 2165–2160 cm^{-1}, which can be ascribable to medium acidic B sites (B_M).[44]

Overall, FT-IR measurements evidence differences in the relative amount and strength of B and L acid sites for the three samples, highlighting for the sample Al–NS–Nit-74 the presence of limited medium strength Lewis sites and the lowest amount of medium-strong Brønsted sites among the three systems.

3.2. Catalytic investigations

All the solids obtained with aluminum nitrate present favorable features for catalytic applications. Their high surface area,

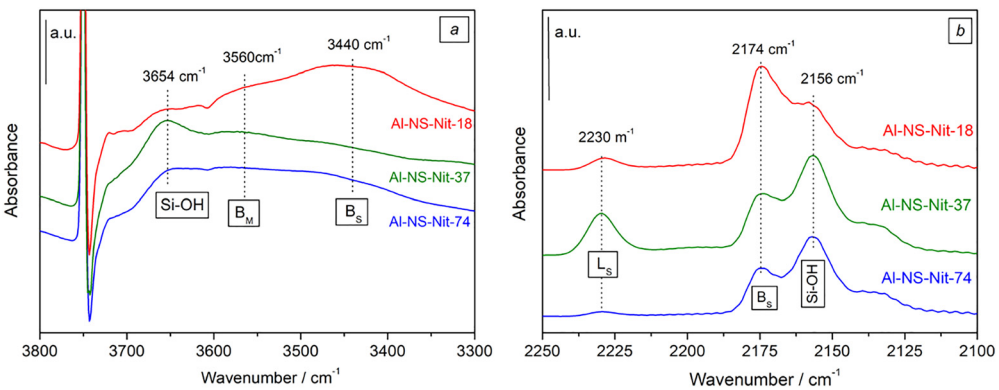

Fig. 7 Normalized IR difference spectra at equal equilibrium pressure (0.1 mbar) of CO at 77 K on Al–NS–Nit-74, Al–NS–Nit-37, and Al–NS–Nit-18 in the high (a) and low frequency region (b). Labels: L_S: strong Lewis, B_S: strong Brønsted, B_M: medium Brønsted.

 © 2026 The Author(s). Published by the Royal Society of Chemistry

Table 3 Catalytic performances of aluminosilicates with different Al precursors and Si/Al ratios for the conversion of glycerol into solketal. Conditions: glycerol : acetone = 1 : 4, 30 mg of catalyst, 50 °C, 2 h, 800 rpm, solvent free

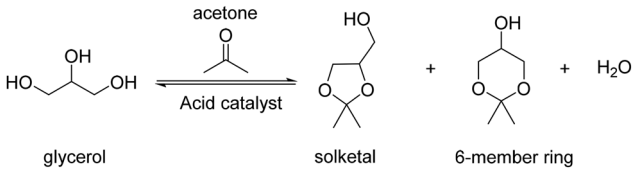

Samples	ICP-OES Si/Al ratio	Yield (%)	Selectivity (%)	Conversion (%)	TON	TON/SSA × 1000
Al–NS–Cl-74	75	18	87	24	322	258
Al–NS–Nit-74	77	17	81	21	350	282
Al–NS–Nit-37	39	23	84	28	200	176
Al–NS–Nit-18	18	20	82	24	160	171

narrow mesopores, spherical particles of extra-small size combined with a high proportion of intra-framework Al make them perfect candidates for the catalytic conversion of glycerol in solketal. Moreover, regarding the acidity measurement reported above, FT-IR analysis of CO adsorption reveals a different population of strong/medium Brønsted acid strength. To correlate the acidity and the catalytic performances, the three solids were tested as catalysts for the conversion of glycerol into solketal and the results are reported in Table 3. For comparison, Al–NS–Cl was tested as well. As expected, the investigations did not reveal any influence of the Al precursor as both Al–NS–Cl-74 and Al–NS–Nit-74 present very close catalytic activity (in terms of turnover number, TON). Interestingly, when comparing the catalytic results of samples Al–NS–Nit-74, Al–NS–Nit-37, and Al–NS–Nit-18, the highest TON was achieved with the Al–Nit-74 catalyst while the sample with the highest quantity of medium-strong Brønsted acid sites (Al–NS–Nit-18) displays the lowest catalytic activity. This result clearly indicates that part of the aluminum present in the materials with a low Si/Al ratio (Al–NS–Nit-37 and Al–NS–Nit-18) is not active. Moreover, Al–NS–Nit-18 gives a lower yield in solketal than Al–NS–Nit-37 (20% *vs.* 23%) for a close selectivity. From these data it could be concluded that part of the Al species present in Al–NS–Nit-18 is even detrimental to the catalytic activity. It should be mentioned that several catalytic tests were performed in duplicate or triplicate, demonstrating excellent reproducibility.

It should be mentioned that the three solids also display a slightly different SSA. However, the different catalytic behavior cannot be entirely ascribed to the differences in SSA, since if the TON divided by the SSA is considered, the highest value is still displayed by the Al–Nit-74 sample (see the last column, Table 3). A possible explanation for this behavior is that the large medium/strong Brønsted acid population present in Al–NS–Nit-18 is causing the products of the reaction to stay strongly bonded to active sites, therefore limiting the catalytic activity. To assess this hypothesis, a kinetic investigation was conducted on both Al–NS–Nit-18 and Al–NS–Nit-74. As predicted, the solid with a Si/Al ratio of 18 displays a slower kinetic in comparison with Al–NS–Nit-74 and its equilibrium

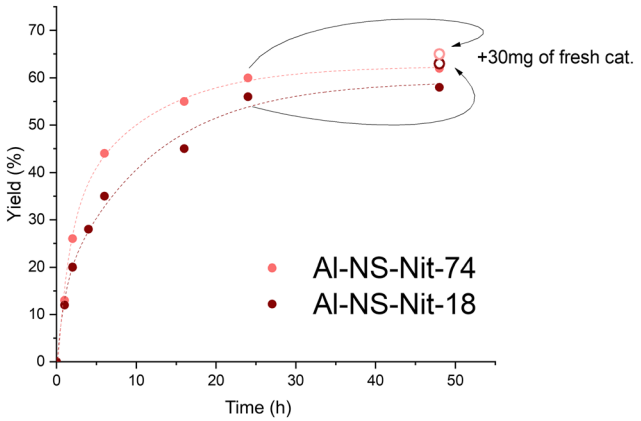

Fig. 8 Kinetic investigations conducted on Al–NS–Nit-74 and Al–NS–Nit-18 for the catalytic conversion of glycerol to solketal. Reaction conditions: glycerol : acetone = 1 : 4, 30 mg of catalyst, 50 °C, 800 rpm, solvent-free. Each point corresponds to one separate catalytic test performed with the same batch of materials. Dotted curves are for eye guidance only.

conversion is decreased (Fig. 8), suggesting a poisoning of the catalyst surface. To confirm the poisoning effect, two additional catalytic tests were performed. After 24 h (at *plateau* conversion), 30 mg of fresh catalyst (Al–NS–Nit-74 and -18) were added to their respective reaction mixture. While the yield in solketal obtained with Al–NS–Nit-74 did not evolve (remaining at thermodynamic equilibrium around 65% of yield), an enhancement of the total conversion of Al–NS–Nit-18 was observed, reaching a similar value to that of Al–NS–Nit-74 (see Fig. 8). This last test allows confirming the poisoning of the Al–NS–Nit-18 catalyst most probably because of the too strong Brønsted acidity. This hypothesis is in line with the results obtained *via* FT-IR of adsorbed CO.

3.3. Al–Ga silicate particles

The highest population of medium/strong Brønsted acid sites can explain the decreased catalytic activity of aluminosilicates with higher Al content (Al–NS-18). Despite Al–NS–Nit-74 is the best catalyst of the series, its catalytic performances were lower in comparison to other solids reported in literature. The difference between the activity of this sample and the one of gallosilicates nanospheres presenting a Si/Ga ratio of 74 and synthesized following a similar procedure was particularly intriguing.[22] To shed light on this interesting behavior, three additional solids were synthesized with different proportions of Ga and Al (see Table 4). Their textural, structural, and morphological properties were investigated with the same techniques employed previously. As expected, their properties are not influenced by the simultaneous presence of two heteroelements. They all display high surface area with narrow pore size distribution (Table 4). The spherical shape and the extra-small size of the particles are preserved (see Fig. S11 for the N_2-physisorption data). The targeted quantities of heteroelements were determined *via* ICP-OES analysis and resulted in agreement with the nominal composition.

© 2026 The Author(s). Published by the Royal Society of Chemistry

Table 4 Physico-chemical properties of bifunctional silica nanospheres synthesized with different quantities of aluminum and gallium

Sample	Si/Al ICP-OES ratio	Si/Ga ICP-OES ratio	Si/X ICP-OES ratio	S_{BET} (m^2 g^{-1})	DFT pore size (nm)	B/L ratio
Al–Ga–NS-148–148	138	155	72	1049	3.2	21
Al–Ga–NS-74–148	67	160	47	1117	3.2	37
Al–Ga–NS-148–74	160	78	119	1122	3.1	6.5

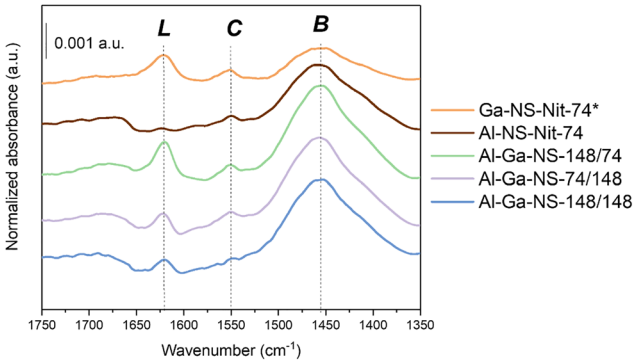

Fig. 9 Difference and normalized FT-IR spectra of ammonia dosages on bi-functional alumino and gallosilicate nanospheres after ammonia dosages and prolonged outgassing at RT. (L: Lewis, B: Brønsted, H: H-bonded, C: Chemisorbed ammonia). *The spectrum of Ga-NS-Nit-74 was previously reported by our group.[22]

The acidity of the samples containing aluminum and gallium was investigated *via* FT-IR of adsorbed ammonia and compared with the one of Al–NS–Nit-74 and Ga-NS-Nit-74 (previously reported[22]) (Fig. 9). The Lewis acid contribution of the bi-metallic samples could be exclusively attributed to the presence of gallium as the peak at 1620 cm^{-1} is not present in Al–NS-Nit-74 and is reduced in the bi-functional materials with a Si/Ga ratio of 148 (Al–Ga–NS-74/148 and Al–Ga–NS-148/148). The Brønsted acidity arises from both the insertion of gallium and aluminum. The introduction of aluminum into the samples causes a rising of the B/L ratio as explained by the "Brønsted character" of Al.[45] Ga-NS-Nit-74 presented the lowest B/L ratio (3.5) among the sample investigated. The bi-metallic samples present both Brønsted and Lewis contributions, their integrated area was used to calculate B/L ratios for the solids and used to correlate their catalytic activity to the acidity properties.

Table 5 summarizes the catalytic performances of the bi-functional materials evaluated for the conversion of glycerol to solketal. For comparison, the catalytic performance of both Al–NS–Nit-74 (entry 1) and Ga–NS–Nit-74 (entry 5) was also included. The mass balance of the catalytic transformation performed with the most active sample of the series (Al–Ga–NS-148–148) was also evaluated (Fig. S12). For this catalyst characterization after the catalytic test was performed as well (Fig. S13). All the catalytic tests were performed under similar reaction conditions (see experimental). As can be seen from the analysis of the data reported in the table, a progressive non-linear increase in solketal yield is observed with the decrease of the B/L ratio. It is known that differences in surface hydrophilicity/hydrophobicity can strongly influence catalytic performances.[22,46] However, due to the very similar features of the different catalysts investigated in this work no relevant differences in terms of surface hydrophilicity are expected. Therefore, the observed trend in catalytic activity clearly indicates that not only the Brønsted acid sites but also the Lewis acidity play a key role in the acetalization reaction. Moreover, as observed previously, too strong B sites are detrimental for the overall catalytic cycles causing a poisoning of the active sites. To complete the overview of the acid properties and enhance the fundamental understanding, a computational study was performed as well.

Table 5 Catalytic performances of alumino-, gallo- and bifunctional silicate nanospheres for the conversion of glycerol in solketal. Conditions: glycerol : acetone = 1 : 4, 30 mg of the catalyst, 50 °C; 2 h, 800 rpm, solvent free

Entry	Samples	Si/X ratio	B/L ratio	Yield (%)	Sel. (%)	Conv. (%)	TON
1	Al–NS–Nit-74	78	ND (mainly B)	17	81	21	350
2	Al–Ga–NS-74–148	47	37	22	85	26	212
3	Al–Ga–NS-148–148	72	21	28	87	32	413
4	Al–Ga–NS-148–74	54	6.5	37	90	41	410
5	Ga–NS-Nit-74[a]	74	3.5	39	90	37	581

[a] Catalytic results obtained with the best gallosilicate nanospheres reported by Maertens *et al.*[22]

3.4. Computational data

The B/L ratios of amorphous aluminosilicates and gallosilicates have been experimentally estimated employing ammonia adsorption monitored by FT-IR. This characterization technique takes advantage of the variations of the vibrational frequencies of the ammonia molecule and of its protonated form (Fig. S14). Vibrational normal modes present in the 1300–1800 cm^{-1} region are generally used, instead of stretching vibrations.

The simulation of the IR spectrum by quantum chemistry methods can help assigning the normal modes to their corresponding bands thus providing additional insights on the structural reason behind the different acidity displayed by the Al- and Ga-based silicates. In its neutral form, the ammonia molecule has three normal modes (one "bending" and two "scissoring") in the 1300–1800 cm^{-1} region, while the ammonium ion has five normal modes in this spectral region (two "bending" and three "scissoring"). The simulated IR spectra of aluminosilicates and gallosilicates are presented in Fig. 10. The comparison between simulated and experimental spectra is intentionally centered around the location of the different peaks. Since the calculated B/L ratios are semi-quantitative, an arbitrary amount of acid sites has been used to

 © 2026 The Author(s). Published by the Royal Society of Chemistry

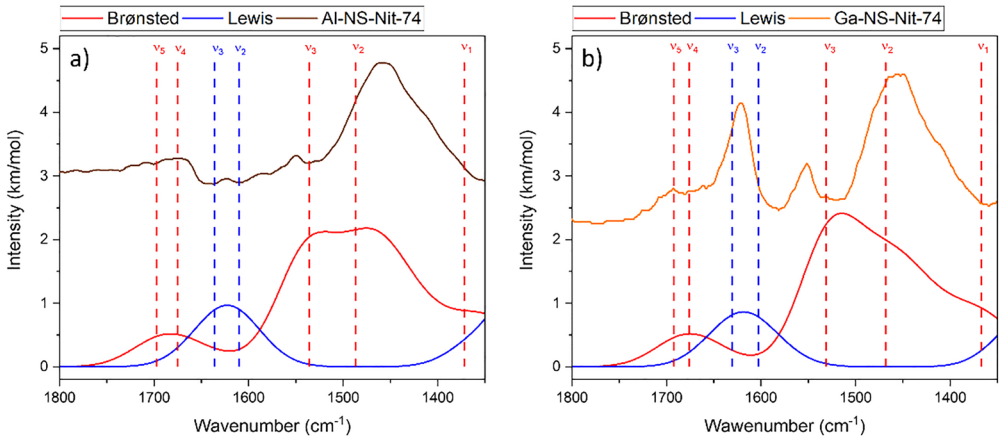

Fig. 10 Comparison between simulated IR spectra of ammonia interacting with Brønsted (red) and Lewis (blue) acid sites in (a) aluminosilicates and (b) gallosilicates, and experimental spectra (brown for aluminosilicates, yellow for gallosilicates). The mean frequency values for each vibrational mode are represented by vertical dashed lines.

model the IR spectra (12 B and 11 L). This does not necessarily reflect the actual composition of the synthesized catalysts, therefore no discussion on the total intensities will be presented. Lewis acid site signature bands are located at 1300 and 1620 cm^{-1}. The first region corresponds to bending motions of the ammonia molecule, while the latter arises from both scissoring modes. For Brønsted acid sites, there are two distinct bands in the 1400–1550 cm^{-1} and 1680–1720 cm^{-1} regions. At the largest wavenumbers, the peak accounts for two of the scissoring modes of the ammonium ion, while the major contributions are observed in the 1400–1600 cm^{-1} region, with three bands corresponding to the two-bending modes and the last scissoring mode.

Though some wavenumber shifts are observed (due to the absence of explicit anharmonicity corrections), the simulated spectra display features comparable to the experimental one thus confirming the validity of the approach employed. Most of the Brønsted and Lewis contributions are distinct. The large band attributed to the Brønsted acid sites observed at 1450 cm^{-1} is attributed to ν_2 and ν_3 vibrational modes of the ammonium ion. The ν_4 and ν_5 vibrational modes are responsible for the smaller peak observed around 1750 cm^{-1}. Regarding Lewis acid sites, the characteristic peak at 1620 cm^{-1} is associated with the second and third vibrational modes. Note that the contribution related to the ν_1 vibration of the ammonia molecule indicated in Table S2 is not observed experimentally because the region below 1300 cm^{-1} is dominated by strong lattice modes of the silica framework that saturate the signal, hence masking the ammonia contribution.

Experimentally, the signature accounting for the presence of Lewis acid sites in the aluminosilicate catalyst is very weak which is interpreted as a larger proportion of Brønsted acid sites. A structural study of the models can provide some indication for the absence of Lewis acid sites in these aluminosilicates. In such materials, the Brønsted acidity usually arises from "pseudo-bridging" silanols. These species consist of tetrahedrally inserted aluminum atoms at the surface, while Lewis acid sites are modeled with a tri-coordinated heteroelement at the surface (Fig. 1). The Si–O bond length amounts typically to 1.6 Å. The insertion of a heteroelement, with a different ionic radius, causes a modification of the bond length. The most affected bond is the one between the Ga or Al atom and the oxygen carrying the acidic proton, called M–O(H). Indeed, in extreme cases, elongation of this bond could lead to a bond dissociation. This shift from a tetra-coordinated to a tri-coordinated structure can be interpreted as the conversion of a Brønsted acid site into a Lewis acid site. As the distance increases, the transition between the two structures becomes more favorable. On average, the Ga–O(H) bond length is 0.1 Å larger than the Al–O(H) bond length. Although it is explained by the difference in ionic radius (Al^{3+} = 0.39 Å and Ga^{3+} = 0.47 Å),[47] this longer bond could facilitate the switching from a Brønsted acid site to a Lewis acid site in the amorphous silica matrix.

The stability of the metal center in its tetrahedral coordination is a major condition for Brønsted acidity. Reineke *et al.*[48] proposed an indicator characterizing the shape of a tetra-coordinated atom, called τ_δ.

$$\tau_\delta = \frac{360 - (\alpha + \beta)}{141}\frac{\beta}{\alpha}$$

where α and β are the two largest O–M–O angles. This τ_δ scale goes from 0 (a square plane) to 1 (a perfect tetrahedron). This indicator is used to assess the structural impact of the insertion of heteroelements in silica structures. As presented in Table 6, the τ_δ value for gallium is slightly inferior to the one for the aluminum insertion meaning that the distortion is larger after the insertion of Ga atoms (values for each site are presented in Table S3). However, the difference between the two τ_δ values is too low to allow a straightforward conclusion. Therefore, to further analyze the relative stabilities of those silica-based catalysts, the energy required to replace a silicon atom with a heteroelement (substitution energy; E_{sub}) was computed according to:

$$E_{sub} = (E_{Si} + E_{Si_{x-1}O_yH_zM}) - (E_M + E_{Si_xO_yH_z})$$

© 2026 The Author(s). Published by the Royal Society of Chemistry

Table 6 Averages M–O(H) distances, τ_δ values, substitution energy, and DPE values for amorphous silica-based catalysts modeled by hemispherical clusters, where M = Al, Ga

M-O(H) (Å)		τ_δ		Substitution energy (kJ mol^{-1})		DPE (kJ mol^{-1})	
Al	Ga	Al	Ga	Al	Ga	Al	Ga
1.905 ± 0.034	2.001 ± 0.047	0.85 ± 0.05	0.83 ± 0.06	−585 ± 46	−270 ± 49	1204 ± 20	1211 ± 28

where E_{Si} and E_{Al} are the DFT energies of the isolated Si^{4+} and M^{3+} ions (M = Al or Ga), $E_{Si_{x-1}O_yH_zAl}$ and $E_{Si_xO_yH_z}$ are the DFT energies of the metal-substituted catalyst and the bare silica cluster with a proton placed on the "acidic" oxygen atom (the geometry of the charged silica cluster has been optimized at the same level as the metal-based catalyst). The E_{sub} values show that the insertion of aluminum in tetrahedral coordination is twice as favorable than the insertion of gallium.

This structural analysis showed that the insertion of aluminum is more favorable and generates a structure closer to a tetrahedron with a shorter Al–O(H) bond length than in gallosilicates. The absence of Lewis acid sites in the synthesized aluminosilicate catalysts can be justified based on the relatively high stability of the Brønsted acid sites formed in the silica matrix after the insertion of an aluminum atom. On the other hand, when a gallium atom is inserted, the structure is more distorted and less stable. Moreover, the elongation of the Ga–O(H) facilitates the switching from a tetra-coordinated to a tri-coordinated structure, corresponding to a Lewis acid.

To go deeper and to understand if the isomorphic substitution of Si with Al or Ga can also induce a difference in the strength of the Brønsted acid sites, further investigations were performed evaluating the deprotonation energy (DPE). The deprotonation energy is a widely used acidity descriptor to characterize the strength of Brønsted solid acids.[49] It corresponds to the energy required to separate the proton of an acid from its conjugate base.

$$\mathrm{DPE} = E_{\mathrm{cat}^-} + E_{\mathrm{H}^+} - E_{\mathrm{catH}}$$

where E_{cat^-} and E_{catH} are the DFT energies of the catalyst under its deprotonated and protonated forms, respectively. Calculations were performed in the gas phase; therefore the DFT energy of the proton is equal to zero. A smaller DPE value corresponds to a stronger Brønsted acidity. DPE values for each cluster are reported in Table 6. For the aluminosilicate clusters, DPE values lie around 1200 kJ mol^{-1}. This is close to what has been computed for zeolites (crystalline aluminosilicates).[50,51] As with the structural properties, the standard deviation represents the diversity of the amorphous materials. The influence of the heteroelement nature on DPE value can be studied by comparing the acid sites individually. Since the acid site models have been prepared with the QM-Opt optimization protocol, the starting geometries of the aluminosilicates and gallosilicates are the same. This allows focusing on the influence of the heteroelement on the DPE. Looking at the energy averages, we can say that aluminosilicates are stronger Brønsted acids than gallosilicates (delta of 7 kJ mol^{-1}). However, probably due to the intrinsic amorphous nature of the selected solids, there are different behaviors within the sample.

The high stability of aluminum in a tetrahedral position within the silica framework along with the lower DPE is consistent with the observed differences in catalytic performance for the conversion of glycerol into solketal. Catalytic investigation has shown that strong Brønsted acid sites tend to have a negative influence on the reaction, whereas the presence of Lewis acid is necessary for good catalytic performance. By providing insights into the low population of Lewis acid sites and stronger Brønsted acidity in aluminosilicate catalysts, quantum chemistry calculations support experimental observations.

4. Conclusions

This study provides a detailed investigation of the acid properties of extra-small aluminosilicate nanospheres and their catalytic performance in the conversion of glycerol to solketal. By optimizing the synthesis conditions, from the choice of aluminum source to Si/Al ratio, it was shown that the dissolution medium critically influences the particle morphology and Al incorporation. Precursors dissolved in ethanol produced homogeneous spherical particles with a high intra-framework Al content, while acidic media led to particle aggregation and distorted Al species. Characterization *via* TEM, ICP-OES, N_2 physisorption, ^{27}Al ssNMR, and FT-IR (NH_3/CO) demonstrated that higher Al content increases acid site density, particularly Brønsted acidity. However, overly strong Brønsted sites led to a decrease in catalytic activity, likely due to catalyst poisoning. For this reason, the best-performing catalyst (Al–NS–Nit-74) exhibited balanced acidity and moderate acid site strength, underlining the importance of accessible, well-tuned active sites. Comparisons with gallosilicate analogues confirmed that Al-containing materials favor Brønsted acidity, whereas Ga-based catalysts provide more Lewis acid sites. Bifunctional Al-Ga systems further allow the fine-tuning of the B/L ratio, revealing that both acid types contribute to the acetalization mechanism. Interestingly, the overall correlation between acidity and catalytic activity clearly indicates that an optimal B/L ratio and relative strength are key parameters for achieving efficient glycerol conversion.

Alongside the experimental characterization, DFT calculations have been employed to rationalize the acidic character of silica-based amorphous catalysts. Lewis and Brønsted acid sites have been modeled with hemispherical clusters carved from

 © 2026 The Author(s). Published by the Royal Society of Chemistry

amorphous silica slabs produced *via* MD. The IR spectra of ammonia adsorbed on each cluster have been simulated and compared to experimental ones, allowing the attribution of the contributions from both acid sites to the total spectrum. Moreover, the absence of Lewis acid sites in the aluminosilicate catalysts has been justified by analyzing the simulated clusters. Compared to Ga, the Al atoms of Brønsted clusters have shorter M–OH bonds, a larger τ_δ index (a better tetrahedral shape), and a larger substitution energy. These properties correspond to more stable tetrahedrons in the amorphous silica matrix, less likely to switch to a Lewis acid site. Finally, computing the DPE after the insertion of Al and Ga atoms showed that aluminosilicate clusters feature stronger Brønsted acid sites.

These findings offer valuable insight into further development of the rational design of heterogeneous acid catalysts, highlighting the critical importance of a tailored synthesis, spectroscopic signature and theoretical modelling in achieving a full understanding of the acidity of metallosilicate nanomaterials for targeted catalytic applications.

Author contributions

A. M., C. R.: conceptualization, data curation, formal analysis, visualization, investigation, methodology, writing – original draft. V. M.: formal analysis, data curation, visualization, writing – original draft. L. S.: investigation. M. A., S. F.: data curation, investigation, supervision, validation, writing – review & editing. C. A., B. C.: funding acquisition, methodology, project administration, resources, supervision, validation, writing – review & editing. All authors have given approval to the final version of the manuscript.

Conflicts of interest

There are no conflicts to declare.

Data availability

The data supporting this article has been included as part of the supplementary information (SI). Supplementary information includes characterization and computational data. Illustration of the sequential MD-QM protocol to compute chemical properties on amorphous silica-based catalyst (Fig. S1), Particle size distribution from TEM (Fig. S2), TEM of Al-NS-Nit-a (Fig. S3), deconvolution of ^{27}Al SSNMR of Al-NS samples prepared using different metal sources (Fig. S4), ^{27}Al ssNMR after different thermal treatment (Fig. S5), N_2-physisorption results (Fig. S6), TEM of samples with different Si/M (Fig. S7), deconvolution of ^{27}Al SSNMR of aluminosilicates samples prepared using different Si/Al molar ratio (Fig. S8), parameters extracted from the lorentzian deconvolution of the ^{27}Al ssNMR MAS spectra (Table S1), FT-IR ammonia dosages (Fig. S9), FT-IR after CO dosages (Fig. S10), N_2-physisorption results bi-functional materials (Fig. S11), mass balance (Fig. S12), Al-Ga-148-148 additional characterization (Fig. S13), graphical representation of computed vibrational modes of ammonia and ammonium (Fig. S14), adsorbed ammonia computed frequencies (Table S2), M-O(H) distances, τ_δ values, substitution energy, and DPE values (Table S3) (PDF). The files containing the atomic cartesian coordinates of the DFT-optimized structures and used for evaluating the DPEs, the substitution energies, and the vibrational spectra are also provided. See DOI: https://doi.org/10.1039/d5ma01361e.

Acknowledgements

The authors thank Dr Luca Fusaro for the fruitful discussions and his support in ssNMR measurements. The authors acknowledge the FNRS for the financial support in the context of the FRIA PhD grants of A. Maertens and L. Soumoy, and the ''Fédération Wallonie-Bruxelles'' for financial support---including the PhD fellowship for C. Rubirigi and V. Marsala—through the ARC program (ARC AC-DC 22/27-127). This project received funding from the FNRS *via* a PdR project (ref: T.0004.21). This research used the resources of PC^2 (Physico-Chemical Characterization) and Electron Microscopy technology platforms located at the University of Namur. The calculations were performed on (i) the computers of the Consortium des Équipements de Calcul Intensif (CÉCI, http://www.ceci-hpc.be) and particularly those of the Technological Platform of High-Performance Computing, for which the authors gratefully acknowledge the financial support of the F.R.S-FNRS, of the Walloon Region, and of the University of Namur (Conventions No. U.G006.15, U.G018.19, U.G011.22, RW1610468, RW/GEQ2016, RW2110213, and RW2210148), and (ii) on Lucia, the Tier-1 supercomputer of the Walloon Region, infrastructure funded by the Walloon Region (grant agreement no. RW1910247). The IR measurements were performed at the Polytechnic of Turin.

References

1 R. Anand, R. Maheswari and U. Hanefeld, *J. Catal.*, 2006, **242**, 82–91.
2 J. C. Bedoya, R. Valdez, L. Cota, M. A. Alvarez-Amparán and A. Olivas, *Catal. Today*, 2022, **388–389**, 55–62.
3 T. Kugita, S. K. Jana, T. Owada, N. Hashimoto, M. Onaka and S. Namba, *Appl. Catal., A*, 2003, **245**, 353–362.
4 N. Lucas, G. Kokate, A. Nagpure and S. Chilukuri, *Microporous Mesoporous Mater.*, 2013, **181**, 38–46.
5 A. Ungureanu, B. Dragoi, V. Hulea, T. Cacciaguerra, D. Meloni, V. Solinas and E. Dumitriu, *Microporous Mesoporous Mater.*, 2012, **163**, 51–64.
6 M. Ravi, V. L. Sushkevich and J. A. van Bokhoven, *Nat. Mater.*, 2020, **19**, 1047–1056.
7 J. Brus, L. Kobera, W. Schoefberger, M. Urbanová, P. Klein, P. Sazama, E. Tabor, S. Sklenak, A. V. Fishchuk and J. Dědeček, *Angew. Chem., Int. Ed.*, 2015, **54**, 541–545.

© 2026 The Author(s). Published by the Royal Society of Chemistry

8 T. Kugita, M. Ezawa, T. Owada, Y. Tomita, S. Namba, N. Hashimoto and M. Onaka, *Microporous Mesoporous Mater.*, 2001, **44–45**, 531–536.
9 A. Satsuma, Y. Segawa, H. Yoshida and T. Hattori, *Appl. Catal., A*, 2004, **264**, 229–236.
10 M. V. Gómez, Á. Cantín, A. Corma and A. de la Hoz, *J. Mol. Catal. A: Chem.*, 2005, **240**, 16–21.
11 A. Styskalik, V. Vykoukal, L. Fusaro, C. Aprile and D. P. Debecker, *Appl. Catal., B*, 2020, **271**, 118926.
12 J.-J. Zou, N. Chang, X. Zhang and L. Wang, *ChemCatChem*, 2012, **4**, 1289–1297.
13 M. J. Gracia, E. Losada, R. Luque, J. M. Campelo, D. Luna, J. M. Marinas and A. A. Romero, *Appl. Catal., A*, 2008, **349**, 148–155.
14 A. Vivian, L. Soumoy, L. Fusaro, P. Louette, A. Felten, S. Fiorilli, D. P. Debecker and C. Aprile, *J. Catal.*, 2021, **400**, 83–92.
15 L. Soumoy, C. Célis, D. P. Debecker, M. Armandi, S. Fiorilli and C. Aprile, *J. Catal.*, 2022, **411**, 41–53.
16 L. Soumoy, A. Morena, M. Armandi, S. Fiorilli, L. Fusaro, D. P. Debecker and C. Aprile, *J. Catal.*, 2025, **447**, 116143.
17 F. Launay, B. Jarry and J. L. Bonardet, *Appl. Catal., A*, 2009, **368**, 132–138.
18 S. Mintova, V. Valtchev, T. Onfroy, C. Marichal, H. Knözinger and T. Bein, *Microporous Mesoporous Mater.*, 2006, **90**, 237–245.
19 A. Maertens and C. Aprile, *Molecules*, 2024, **29**, 102.
20 Z. Luan, C.-F. Cheng, W. Zhou and J. Klinowski, *J. Phys. Chem.*, 1995, **99**, 1018–1024.
21 N. Godard, X. Collard, A. Vivian, L. A. Bivona, S. Fiorilli, L. Fusaro and C. Aprile, *Appl. Catal., A*, 2018, **556**, 73–80.
22 A. Maertens, A. Vivian, L. Fusaro, A. Felten, P. Louette, M. Armandi, S. Fiorilli and C. Aprile, *Sustainable Energy Fuels*, 2022, **6**, 3818–3829.
23 L. Li, D. Cani and P. P. Pescarmona, *Inorg. Chim. Acta*, 2015, **431**, 289–296.
24 X. Collard, L. Li, W. Lueangchaichaweng, A. Bertrand, C. Aprile and P. P. Pescarmona, *Catal. Today*, 2014, **235**, 184–192.
25 E. Janiszewska, J. Kowalska-Kuś, J. Wiktorowska, A. Jankowska, A. Tabero, A. Held and S. Kowalak, *Molecules*, 2024, **29**, 5512.
26 J. Diwakar, B. Saini, A. P. Tathod, S. Arumugam, G. Gaur and N. Viswanadham, *ACS Sustainable Resour. Manage.*, 2025, **2**, 1859–1868.
27 M. Thommes, K. Kaneko, A. V. Neimark, J. P. Olivier, F. Rodriguez-Reinoso, J. Rouquerol and K. S. W. Sing, *Pure Appl. Chem.*, 2015, **87**, 1051–1069.
28 D. Massiot, F. Fayon, M. Capron, I. King, S. Le Calvé, B. Alonso, J.-O. Durand, B. Bujoli, Z. Gan and G. Hoatson, *Magn. Reson. Chem.*, 2002, **40**, 70–76.
29 C. Rubirigi, C. Aprile and B. Champagne, *Adv. Theory Simul.*, 2026, **9**, e01609.
30 C. Vandervelden, A. Jystad, B. Peters and M. Caricato, *Ind. Eng. Chem. Res.*, 2021, **60**, 12834–12846.
31 A. Jystad, H. Leblanc and M. Caricato, *J. Phys. Chem. C*, 2020, **124**, 15231–15240.
32 M. J. Frisch, G. W. Trucks, H. B. Schlegel, G. E. Scuseria, M. A. Robb, J. R. Cheeseman, G. Scalmani, V. Barone, G. A. Petersson, H. Nakatsuji, X. Li, M. Caricato, A. V. Marenich, J. Bloino, B. G. Janesko, R. Gomperts, B. Mennucci, H. P. Hratchian, J. V. Ortiz, A. F. Izmaylov, J. L. Sonnenberg, D. Williams-Young, F. Ding, F. Lipparini, F. Egidi, J. Goings, B. Peng, A. Petrone, T. Henderson, D. Ranasinghe, V. G. Zakrzewski, J. Gao, N. Rega, G. Zheng, W. Liang, M. Hada, M. Ehara, K. Toyota, R. Fukuda, J. Hasegawa, M. Ishida, T. Nakajima, Y. Honda, O. Kitao, H. Nakai, T. Vreven, K. Throssell, J. A. Montgomery Jr., J. E. Peralta, F. Ogliaro, M. J. Bearpark, J. J. Heyd, E. N. Brothers, K. N. Kudin, V. N. Staroverov, T. A. Keith, R. Kobayashi, J. Normand, K. Raghavachari, A. P. Rendell, J. C. Burant, S. S. Iyengar, J. Tomasi, M. Cossi, J. M. Millam, M. Klene, C. Adamo, R. Cammi, J. W. Ochterski, R. L. Martin, K. Morokuma, O. Farkas, J. B. Foresman and D. J. Fox, *Gaussian 16 Rev. C.01*, 2016.
33 S. Grimme, *Wiley Interdiscip. Rev.: Comput. Mol. Sci.*, 2011, **1**, 211–228.
34 F. Weigend and R. Ahlrichs, *Phys. Chem. Chem. Phys.*, 2005, **7**, 3297–3305.
35 A. Vivian, L. Soumoy, L. Fusaro, P. Louette, A. Felten, S. Fiorilli, D. P. Debecker and C. Aprile, *J. Catal.*, 2021, **400**, 83–92.
36 F. Rouquerol, J. Rouquerol and K. Sing, Adsorption by Powders and Porous Solids - Principles, Methodology and Applications, Elsevier, 1999.
37 C. Sangwichien, G. L. Aranovich and M. D. Donohue, *Colloids Surf., A*, 2002, **206**, 313–320.
38 M. Haouas, F. Taulelle and C. Martineau, *Prog. Nucl. Magn. Reson. Spectrosc.*, 2016, **94–95**, 11–36.
39 Z. Zhao, S. Xu, M. Y. Hu, X. Bao, C. H. F. Peden and J. Hu, *J. Phys. Chem. C*, 2015, **119**, 1410–1417.
40 M. Ravi, V. L. Sushkevich and J. A. van Bokhoven, *J. Phys. Chem. C*, 2019, **123**, 15139–15144.
41 A. J. J. Koekkoek, J. A. R. van Veen, P. B. Gerrtisen, P. Giltay, P. C. M. M. Magusin and E. J. M. Hensen, *Microporous Mesoporous Mater.*, 2012, **151**, 34–43.
42 Z. Wang, Y. Jiang, A. Baiker and J. Huang, *Acc. Chem. Res.*, 2020, **53**, 2648–2658.
43 O. Cairon, T. Chevreau and J.-C. Lavalley, *J. Chem. Soc., Faraday Trans.*, 1998, **94**, 3039–3047.
44 G. Crépeau, V. Montouillout, A. Vimont, L. Mariey, T. Cseri and F. Maugé, *J. Phys. Chem. B*, 2006, **110**, 15172–15185.
45 M. Shamzhy, M. Opanasenko, P. Concepción and A. Martínez, *Chem. Soc. Rev.*, 2019, **48**, 1095–1149.
46 A. Vivian, L. Soumoy, L. Fusaro, S. Fiorilli, D. P. Debecker and C. Aprile, *Green Chem.*, 2021, **23**, 354–366.
47 R. D. Shannon, *Acta Crystallogr., Sect. A*, 1976, **32**, 751–767.
48 M. H. Reineke, M. D. Sampson, A. L. Rheingold and C. P. Kubiak, *Inorg. Chem.*, 2015, **54**, 3211–3217.
49 P. Deshlahra and E. Iglesia, *Chem. Commun.*, 2020, **56**, 7371–7398.
50 M. Boronat and A. Corma, *ACS Catal.*, 2019, **9**, 1539–1548.
51 A. J. Jones, R. T. Carr, S. I. Zones and E. Iglesia, *J. Catal.*, 2014, **312**, 58–68.

© 2026 The Author(s). Published by the Royal Society of Chemistry